Research Article | Vol. 33, No. 5 / 10 Mar 2025 / Optics Express 10006
Optics EXPRESS

High-average-power, few-cycle, 2.1 µm OPCPA laser driver for soft-X-ray high-harmonic generation

DANIEL WALKE,[1] AZIZE KOÇ,[1] FLORIAN GORES,[1] MINJIE ZHAN,[2] NICOLAS FORGET,[3,4] RAMAN MAKSIMENKA,[3] AND IAIN WILKINSON[1,*]

[1] *Helmholtz-Zentrum Berlin für Materialien und Energie GmbH, Hahn-Meitner-Platz 1, 14109 Berlin, Germany*
[2] *UltraFast Innovations GmbH, Dieselstr. 5, 85748 Garching (Munich), Germany*
[3] *FASTLITE, 165 rue des Cistes, 06600 Antibes, France*
[4] *Current address: Université Côte d'Azur, CNRS, Institut de Physique de Nice (INPHYNI), UMR 7010, 17 rue Julien Lauprêtre, 06200 Nice, France*
[*] *iain.wilkinson@helmholtz-berlin.de*

Abstract: Repetition-rate upscaling of intense, femtosecond-duration pulses in the short-wave infrared is necessary to further develop and apply tabletop, ultrafast soft-X-ray sources. Here, we present a 20 fs-pulse-duration, 2.1 µm-central-wavelength, optical parametric chirped-pulse amplification laser, which outputs 52 W of amplified signal power at a repetition rate of 52.6 kHz. Despite the potential for deleterious thermal processes, the laser output exhibits excellent spatial and temporal profiles in a 45 W beam at a soft-X-ray-generation target after ~5 m of propagation. In argon gas, this enables high-harmonic generation up to ~190 eV photon energies, demonstrating the system's potential for ultrashort soft-X-ray-pulse production.

1. Introduction

There is great interest in developing high-average-power lasers capable of delivering millijoule-level, femtosecond-duration pulses in the short-wave infrared (SWIR, ~1.4–3.0 µm) spectral region as drivers for high-order-harmonic generation (HHG) [1–4]. Compared to commonly used near-infrared (NIR) HHG driving lasers, SWIR drivers increase the photon cut-off energy, which scales with λ^2 [5,6]. Accordingly, multiple SWIR systems are now in operation worldwide, producing ultrafast, coherent and broadband HHG outputs extending well into the soft X-ray (SXR) spectral range [2,3,7–14]. A driving wavelength of ~1.8 µm is sufficient to cover the transparency window in water between the carbon and oxygen K edges. With a 3.9 µm driver, output photon energies in excess of 1 keV have been reported [15]. In principle, the resulting attosecond-to-few-femtosecond-duration SXR pulses promise to be powerful spectroscopic probes: sensitive to the local chemical environment at specific elemental sites, brief enough to capture the fastest dynamics in matter and implementable in a typical research laboratory for studies in gases [16,17], solids [18,19] and liquids [20]. Yet, in practice, the SWIR-to-SXR energy conversion efficiency is very low — on the order of 10^{-11} per 1% bandwidth around the carbon K edge [7,10,12] — and, with currently available light sources, a correspondingly low on-target photon flux represents a significant limitation [20,21].

Although strategies to improve the HHG yield are an active area of research [22–24], the most direct route to brighter SXR beams is to scale up the laser-pulse repetition rate, and so the average power. In this regard, two platforms have emerged that offer both high peak and

#547689 https://doi.org/10.1364/OE.547689
Journal © 2025 Received 11 Nov 2024; revised 17 Jan 2025; accepted 30 Jan 2025; published 26 Feb 2025

Optics EXPRESS

average power: NIR-pumped optical parametric chirped-pulse amplifiers (OPCPAs) [2–4,25,26] — the subject of the present work — and non-linear compression of the outputs of thulium-doped fiber chirped-pulse amplification (Tm:FCPA) lasers. In the latter case, a remarkable combination of 1.3 mJ, 10.2 fs and 1.9 μm central wavelength pulses with a repetition rate of 100 kHz (130 W average power) has recently been demonstrated [27]. OPCPAs, on the other hand, are pulse-energy scalable, wavelength-tuneable and can directly produce high-contrast, few- (or even single-) optical-cycle pulses without the need for non-linear spectral broadening [2–4,28]. Furthermore, carrier-envelope-phase (CEP) stability, a crucial property for HHG driven by few-cycle pulses [7], is preserved during optical parametric amplification and has been achieved in many SWIR-OPCPAs, including at high peak and average powers [4,25].

In an OPCPA, a broadband but chirped seed pulse is parametricly amplified by a high-energy, higher frequency pump pulse of comparable duration within a suitable non-linear optical crystal [29]. Together with rapid developments of Yb:YAG-based picosecond lasers, OPCPA approaches have been applied to generate millijoule-level, femtosecond-duration SWIR pulses at repetition rates in the range of 10–100 kHz with few-tens-of-W average powers [30] — far beyond the 0.01–1 kHz and <2 W range employed in the first generation of SXR-HHG sources [1,7,10,12]. A principal challenge in such OPCPA developments is maximizing the pump-to-signal conversion while maintaining broadband amplification and avoiding significant temporal, spectral and spatial distortions. To achieve efficient, broadband amplification, thin optical crystals are exposed to high peak intensities and average powers. Spatial, spatio-temporal and spatio-spectral distortions due to saturation and coinciding non-linear processes are well documented in optical parametric amplifiers (OPAs) and OPCPAs [31]. These issues are compounded at high average powers by the associated thermal loads on the crystals [32]. Additionally, the high thermal loads at subsequent optics and in beam-transport lines can lead to further beam degradations, which have particularly severe consequences when driving high-order non-linear optical processes. For example, considering SXR-HHG, poor focusability and/or temporal compressability of the driving pulses will reduce conversion efficiencies, since less of the total pulse energy will contribute to the SXR emission. Furthermore, pulses with irregular or modulated spatial profiles may be susceptible to beam breakup within the gas medium employed for SXR-HHG [10,13]. Correspondingly, high-power SWIR laser systems with excellent spatio-temporal properties are required to fully leverage the average-power gains of modern pump lasers for SXR-HHG.

An OPCPA with an output spectrum centered around 2.1 μm and pumped at the Yb:YAG lasing wavelength of 1030 nm operates near degeneracy (i.e., $\lambda_{\text{signal}} = \lambda_{\text{idler}}$), enabling broadband phase matching in a quasi-collinear interaction geometry; a small angle is necessary between the seed and pump beams to separate the oppositely-chirped and potentially interfering signal and idler beams from each other and these beams from the depleted pump beam at the non-linear-crystal output. Two notable examples of such near-degenerate, high-average-power OPCPAs driving water-window SXR-HHG sources are a 25 W system with 16 fs-duration pulses and a 100 kHz repetition rate [2], and a 27 W system with 27 fs pulses and a 10 kHz repetition rate [3]. A 10 kHz, CEP-stable system generating 49 W and pulses compressible down to 20 s [4] and a 50 kHz system generating 50 W and down to 38 fs pulses [33] were also recently reported, although HHG was not yet demonstrated with these systems.

Here, we describe a high-average-power, SWIR (2.1 μm), ultrashort-pulsed (20 fs full-width at half-maximum, FWHM, duration) and high-repetition-rate (52.6 kHz) OPCPA pumped by a 500 W Yb:YAG thin-disk laser and seeded by a passively CEP-stable front end. The system generates 52 W of average amplified signal power with no significant energy loss to parasitic processes, resulting in an on-target power of 45 W for SXR-HHG. The high average power induces a thermal gas lens when propagated through air, which is suppressed by purging the beam path with N_2 gas. With such purging, an excellent beam quality (M^2) is maintained over a ~5 m propagation length, as determined through measurements of the full focal beam caustic.

Optics EXPRESS

Preliminary CEP-stability measurements of the full system output are presented. Furthermore, to verify the OPCPA system performance, and as a first step towards a high-photon-flux water-window spanning source, high harmonics are generated in an argon-filled gas cell up to 190 eV photon energies.

2. OPCPA layout and front end

The layout of the OPCPA is depicted in Fig. 1. The system is pumped by a Yb:YAG thin-disk regenerative amplifier (DIRA 400-50, upgraded to 500 W, Trumpf Scientific Lasers GmbH + Co. KG.), which is seeded by a Yb:YAG fiber oscillator and three-stage amplifier laser with a temporally chirped output (TruMicro 2000, Trumpf Scientific Lasers GmbH + Co. KG.). The complete pump-laser system outputs 9.6 mJ, 1030 nm-wavelength pulses of 850 fs (FWHM) duration at a repetition rate of 52.6 kHz. The pump laser offers an average M^2 of 1.2 (according to ISO 11146, with <10% astigmatism), a 0.5–0.6% RMS shot-to-shot energy stability, and a 0.2% RMS average-power stability. The 1030 nm pump-laser beam pointing is stabilized after the output port by a two-channel, piezo-actuated stabilization system (MRC Systems GmbH). The OPCPA system occupies a 2.5 × 1.5 m^2 optical-table space and is split into two parts: a commercial OPCPA (Starzz, Fastlite), which acts as a front end and consumes 50 W of the pump power to generate broadband-signal pulses at an average power of 5.3 W, and a two-stage high-power booster, which amplifies this output to over 50 W after the final OPA stage. Most of the thin-disk laser power, 415 W, pumps the high-power stages, while the remainder is reserved for the development of a synchronized pump-pulse source. To ensure long-term thermo-mechanical stability, the two sections of the OPCPA (front-end and high-power booster) are enclosed in separate but mechanically conjoined, gas-purgeable aluminum enclosures, each containing a water-cooled breadboard.

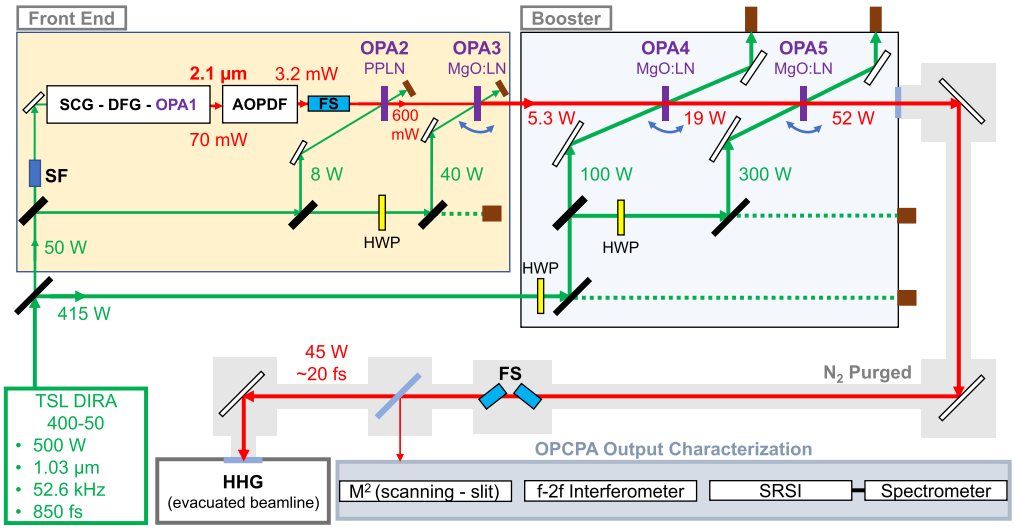

Fig. 1. Schematic layout of the laser system. The green and red lines show the 1.03 µm pump and 2.1 µm signal beams, respectively. Adjustable half waveplates (HWPs) placed before thin-film polarizers (black rectangles) enable attenuation of the pump pulse energy at OPAs 3-5. The idler beams generated in OPAs 2-5 are dumped after each stage and are not shown in the schematic. TSL, Trumpf Scientific Lasers; SF, spatial filter; SCG, supercontinuum generation; DFG, difference-frequency generation; AOPDF, acousto-optic programmable dispersive filter; FS, bulk fused silica; PPLN, periodically poled lithium niobate; MgO:LN, MgO-doped lithium niobate; SRSI, self-referenced spectral interferometry.

Optics EXPRESS

The seed-generation scheme is similar to those presented in Refs. [34] and [3]. Broadband 2.1 μm pulses are formed by difference-frequency generation (DFG) between the short wavelength side of a supercontinuum, as seeded by a fraction of the pump pulse, and a second, low-energy replica of the pump pulse. The resulting broadband, negatively chirped 2.1 μm idler pulses are then amplified to 1.5 μJ in a 1 mm-thick, MgO-doped periodically-poled lithium niobate (PPLN) crystal (OPA 1, type 0, fan-out poling period around 31 μm). Although such DFG schemes theoretically result in CEP stable pulses, this has not always been observed in practice, particularly when pumped by a high-average power laser [3]. The degradation or absence of CEP stability in these cases has been attributed to fluctuations in the pump spatial profile [35]. In an attempt to mitigate these fluctuations, the combined pump for the SCG-DFG-OPA1 stages is first propagated through a hollow-core capillary (100 mm length, 90-95% transmission efficiency) [36].

The pulses from OPA 1 are sent to a high-repetition-rate acousto-optic programmable dispersive filter (AOPDF; Dazzler UHR-1600-2700, Fastlite) for control over the spectral phase, amplitude, and CEP. As the diffraction efficiency of the pulse shaper is greater when applying a high group-delay dispersion (GDD), the negatively-chirped idler pulses from OPA 1 are first stretched by adding +11000 fs^2 of GDD in the pulse shaper, before they are partially re-compressed in a 50 mm-long bulk-fused-silica block. This leaves a residual SWIR GDD of +3000 fs^2, which results in a pulse duration of ~400 fs. Amplifying a positively chirped seed is desirable because it allows the high-energy pulses to be compressed in bulk fused silica after the OPCPA booster. Performing this additional pulse lengthening and partial compression also results in an increase in the AOPDF diffraction efficiency and pulse-shaper transmission by 30% (specifically when accounting for the additional reflective losses on the added, uncoated bulk-fused-silica surfaces). The energy in the SWIR pulses after shaping is 45 nJ.

The remainder of the OPCPA front-end consists of two more amplification stages. In the first (OPA 2, type 0), the seed pulses are amplified to 10 μJ (0.53 W) in a 1 mm-thick, PPLN crystal (30.7 μm poling period) by 150 μJ (7.9 W) pump pulses. Although PPLN demonstrates an enhanced non-linear coefficient and amplification bandwidth in a type 0 (quasi) phase-matching geometry in comparison to type-1, bulk, MgO-doped lithium niobate (LN), PPLN is not available in the large apertures required for the high-power amplification stages. Therefore, the final front-end stage (OPA 3, type 1) incorporates a 1.5 mm-thick bulk LN crystal (Θ=45.4° and Φ=30° cut angles), where the signal-beam pulse energy is further increased to 100 μJ (5.3 W) using 766 μJ (40.3 W) pump pulses with a 110 GW/cm^2 peak intensity at the crystal. Generally, photo-refraction in LN can lead to crystal damage at relatively moderate intensities, motivating the search for alternative crystal types in high-power SWIR OPCPAs [3]. In the OPCPA system presented here, the PPLN and bulk-LN crystals are all MgO-doped [37] and heated and stabilized to ~120°C [38] to suppress the photo-refractive effect.

Before the development of the high-power booster, the CEP stability of the OPCPA front end was verified. The 100 μJ output pulses were compressed using a pair of chirped mirrors (PC1741, Ultrafast Innovations GmbH, -250 fs^2 per reflection and 10 reflections) before a portion was sent to an 'f-2f' interferometer coupled to a fast read-out system (Fringeez, Fastlite). A shot-resolved CEP phase stability of ~160 mrad RMS was measured over a 25-minute period at a read-out rate of 13.15 kHz (i.e., every fourth pulse was measured) [39], as further discussed at the end of Section 4.

3. High-average-power booster

To maximize reflectivity and minimize thermal loads from the high-power 1030 nm beams applied in the high-power booster system, highly reflective (>99.98% reflectivity) dielectric mirrors and beam splitters, specifically designed for high-average-power and ultrashort-pulse NIR beams, are implemented for pump-beam routing. Furthermore, SWIR-enhanced Ag mirror coatings and

Optics EXPRESS

thermally conductive crystalline-silicon substrates are adopted for the high-power SWIR beams generated in the booster system. This importantly reduces thermal loads on and/or behind the optical substrates and thermal-lensing effects at the high-power-mirror surfaces. Additionally, all back-reflections from the transmissive optics are dumped using water-cooled beam blocks. Finally, following the bulk LN OPA stages, the residual pump and generated idler beams are dumped using independently water-cooled beam dumps mounted to the external sides of the monolithic, water-cooled aluminium laser enclosure. Collectively, these measures engender excellent OPCPA-system shot-to-shot energy and power stabilities, as further discussed below.

The high-power booster OPCPA section consists of two further bulk-LN amplification stages, OPAs 4 and 5. Splitting the high-power amplification into two separate stages reduces the signal gain at each stage. A lower gain is associated with a higher pump-to-signal conversion efficiency since more power can be extracted before back-conversion becomes significant. Furthermore, a greater amplification bandwidth is achievable since thinner crystals can be used. Compared to using completely separate pump beams for individual OPCPA stages, higher pump extraction efficiencies have been reported in designs employing pump recycling [40], in which the full pump power is sent to a first (unsaturated) OPA stage and the remaining power is then used to pump a second stage. However, in this case, self-focusing of the high-power pump in the bulk-LN OPA 4 crystal made the beam unsuitable for use in the subsequent amplification stage. Such lensing could be induced in the OPA 4 crystal by either the high average power (i.e., thermal lensing) or peak intensity (i.e., Kerr lensing); no tests were made to distinguish between these processes. Although recovering the correct pump beam size and divergence would have been theoretically possible with a suitably tuned telescope, such a scheme was impractical as the power of the induced lens in the OPA 4 crystal was not constant but rather strongly dependent on the degree of pump depletion (i.e., when the amplification was fully optimized, the lensing effect was weaker). Therefore, we chose to split the pump power before the booster amplification stages (OPA stages 4 and 5). Although the theoretically expected extraction is lower, the complexity of achieving and maintaining the optimal pump beam shape and intensity at each stage is significantly eased, with the additional advantage that the overall thermal load at each LN crystal is reduced.

After a reflective demagnifying telescope, the 415 W of pump power sent to the high-power booster is split in a ratio of 1:3 between the OPA 4 and 5 stages. Although 5.3 W of seed power is generated from the front end, this drops to 4.6 W after the unpumped OPA 4 stage due to reflective losses on the LN crystal surfaces, despite the presence of an anti-reflection (AR) coating. The remaining power is amplified to 19.0 W in a 1.5 mm-thick bulk-LN crystal (Θ=45.4° and Φ=30° cut, ~100 W pump power, 73 GW/cm^2 pump beam intensity, 2.9 mm and 3.5 mm respective 1/e^2 pump and seed beam diameters). The input beams cross at the crystal in the phase-matching plane at an angle of 2.9° (external, corresponding to a ~1.3° internal angle). This angle is orientated in the 'tangential' or 'non-walk-off compensating' phase-matching geometry [41], specifically to maximise the phase-matched bandwidth and suppress parasitic second-harmonic generation of the amplified 2.1 µm pulses. The small crossing angle is critical for broadband amplification. An external crossing angle of 4.5° resulted in no amplification at wavelengths below 1950 nm and a signal-beam output power of only 16.5 W. Reducing the crossing angle to less than 2.9° resulted in no further improvement. Due to thermal lensing in the LN crystal, a higher pump intensity was not possible without risking damage to the pump-extraction mirrors, which direct the depleted pump beam to a water-cooled beam dump after the OPA stage.

The final amplification stage (OPA 5) is based on another 1.5 mm-thick bulk-LN crystal (Θ=45.4° and Φ=30° cut). The pump power and intensity are respectively set to ~300 W and 76 GW/cm^2 (average 1/e^2 beam diameter of 4.6 mm) and the pump and seed beams again cross at an angle of 2.9° (external) in the non-walk-off compensating geometry. After optimization (spatial superposition, pump-seed delay and crystal angle) 15.7 W of seed power (transmission of the OPA 4 power through the unpumped OPA 5 crystal) is amplified to 52 W, corresponding

Optics EXPRESS

to a pump-to-signal conversion of 11.9%. During the OPCPA development, it was necessary to increase the signal beam size at the first signal mirror after OPA 5 to avoid laser-induced damage. This was accomplished by operating the stage with a diverging seed ($1/e^2$ beam diameter of 6.5 mm at the crystal plane), set by a f=-500 mm concave mirror. Despite the seed being significantly larger than the pump, reducing the seed size resulted in a decreased signal power.

The occurrence of mirror damage following OPA 5 indicated that the signal beam was, similar to the 1030 nm pump beam, subject to lensing within the last LN crystal. This was confirmed by visualizing a weak replica of the OPA 5 signal output via two-photon absorption in a silicon-based CMOS camera; a bandpass filter (Thorlabs BP2250-500) was installed in front of the camera. The signal-beam size significantly reduced as the pump power at OPA 5 was increased. When the timing between the pump and seed pulses was fully detuned and equivalent crystal pump powers were applied to the crystal, similar beam size reductions were observed for the transmitted, unamplified seed beam, thus demonstrating that the induced lensing is a predominantly thermal effect.

The gain and pump-to-signal extraction for the three bulk-LN stages (including the final stage of the OPCPA front end) are plotted as a function of pump intensity in Fig. 2(a), (b) and (c). In each case, it is necessary to tune the crystal angle for optimal phase-matching as the pump pulse energy is increased and the crystal temperature rises. Each of the LN stages is operated in a saturated regime but before the onset of significant back conversion. This is reflected in Fig. 2(a)–(c) by the pump-extraction curves, which maintain their maximum values up to their full operating intensities. The degree of gain saturation was carefully engineered in each LN stage to balance energy-stability gains versus deleterious back-conversion effects and beam-profile degradations.

The key operating parameters of the bulk-LN OPA stages are summarised in Table 1. The advantage of operating the high-power amplification stages with a low gain is demonstrated by the impressive 14.4% pump-to-signal-extraction (~30% quantum efficiency, QE) in OPA 4. Furthermore, this figure indicates that there is scope to further upscale the output signal power by realizing a similar extraction ratio and QE in OPA 5. The lower efficiency of OPA 5 likely has two origins. First, the non-collinear pump-seed angle and larger input beam diameters implemented in OPA 5 lead to greater spatio-temporal walkoff effects, limiting the achievable extraction ratio [29]. Second, the thermally induced beam reshaping that occurs in OPA 5 leads to a crystal-depth-dependent mismatch between the seed and pump beam sizes, impeding optimal energy transfer between the pump and signal fields. While the former walkoff effect is inherent to the implemented phase-matching scheme, we believe that the pump- and seed-beam mode matching in OPA 5 can still be improved, allowing a higher pump-to-signal power extraction to be achieved. In addition, a further increase of the output signal power would be possible with improved AR coatings on the LN-crystal surfaces, each of which currently impose a 6% reflective loss on the 2.1 μm-wavelength beam.

Table 1. Comparison of the pump parameters and signal-amplification performance for the three bulk-LN OPA stages. P_{pump}, I_{peak}, and QE are the respective average pump powers, pump peak intensities, and quantum efficiencies achieved at each crystal.

OPA	P_{Pump} (W)	I_{Peak} (GW/cm^2)	Gain	Extraction (%)	QE (%)
3	40	101	9.5	12.0	25
4	100	72	4.1	14.4	30
5	300	78	3.2	11.9	25

To check for the presence of parasitic second-harmonic generation or stress-induced depolarization in the amplification stages, the OPA-5-output signal beam was sampled by a normal incidence reflection from a CaF_2 wedged window, and the low-power beam was collected

Optics EXPRESS

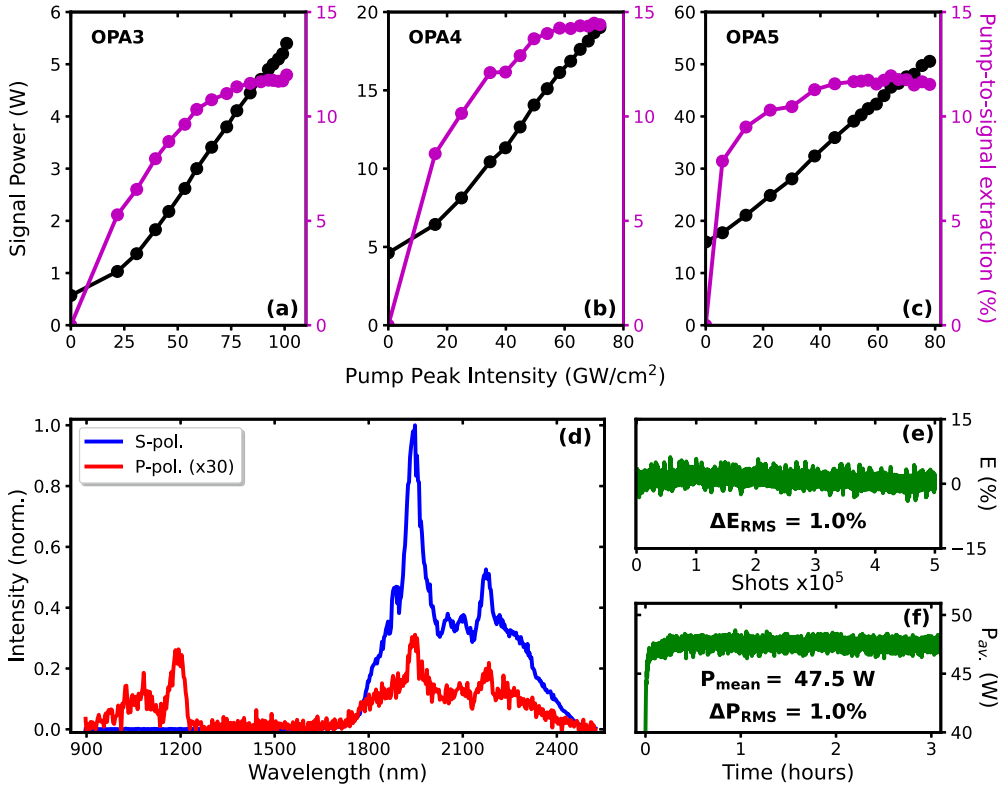

Fig. 2. (a), (b), (c) Signal gain and pump-to-signal extraction at OPA stages 3, 4 and 5, respectively. (d) Spectra of the OPA-5-output s- and p-polarized signal-beam components. (e) Shot-to-shot energy and (f) average-power stability measurements of the OPA-5-output signal pulses. S-pol., P-pol., E, ΔE_{RMS}, $P_{av.}$, P_{mean}, and ΔP_{RMS} refer to s-polarization, p-polarization, pulse-energy deviation, root-mean-square pulse-energy fluctuation, instantaneous average power, mean measured power, and root-mean-square average-power fluctuation, respectively.

by an integrating sphere, fibre-coupled to an actively cooled, extended InGaAs spectrometer (NIRquest+2.5, Ocean Optics Inc.). The spectra were recorded through a polarizer (Thorlabs LPNIRA050-MP2) set to either pass s- or p-polarized light (see Fig. 2(d)). Although the integrating sphere and InGaAs-sensor combination attenuates the long wavelength side of the signal spectrum (leading to the disparity between the spectra shown in Figs. 2(d) and 3(d)), it has the advantage of being insensitive to beam alignment and polarization. To prevent damage to the polarizer, the AOPDF was used to reduce the seed pulse repetition rate by a factor of four, while all other conditions remained the same. Over 95% of the output power is contained in the primary s-polarized 2.1 µm spectrum, with the residual power being p-polarized and distributed between a small sum-frequency-generated peak close to 1200 nm and a weak orthogonally polarized replica of the signal beam.

The shot-to-shot energy stability of the signal output of OPA 5 is shown over 500,000 laser shots (~10 s) in Fig. 2(e), where it is plotted as a percentage of the deviation from the average ~1 mJ output, highlighting a 1.0% RMS deviation. The OPA-5-signal output power is sustained at over 50 W over a period of several hours. However, due to the high thermal load, it is not possible to sustainably measure the output signal power from OPA 5 using low-profile, passively cooled power-measurement sensors. Furthermore, the low beam heights implemented in the OPCPA

Optics EXPRESS

system prevent direct measurements with large, actively cooled devices. Hence, long-term power measurements are performed after four additional optics using a water-cooled power head (1000WP-BB-34, Ophir Optronics Solutions Ltd.). An associated and characteristic data set, recorded at 1 Hz, is shown in Fig. 2(f). Directly after pumping OPA5, a sustained 47.5 W average power is measured with a 1.0% RMS stability after four optics and over a more than three-hour measurement time.

4. Output-pulse characterization

The OPCPA-system output is collimated at a $1/e^2$ beam diameter of ~11 mm by an f=2000 mm concave mirror, resulting in a ≤0.1 mrad divergence; an iris placed in front of a thermoelectric power meter (UP55N-100H-H9-D0, Gentec Electro-Optics Inc.) was used to estimate the beam size. The beam is subsequently transported to our evacuated SXR-HHG beamline using SWIR-enhanced Ag mirrors on thermally conductive crystalline silicon substrates and under a N_2-purged atmosphere (<5% relative humidity) over a ~5 m distance. Reflections from two, 3 mm-thick CaF_2 wedged windows placed in the beam close to the SXR-HHG setup provide separate, low-energy pulse replicas for beam and pulse characterization. The associated OPCPA-output beam profiles and the beam caustic were measured using a commercial scanning slit beam profiler (NanoScan 2s Pyro/9/5, Ophir Optronics Solutions Ltd.). Due to the limited 9 mm aperture of the beam profiler, the collimated-OPCPA-output beam profile was measured after a 3:1 demagnifying telescope at a ~5 m distance from OPA 5. The resulting super-gaussian vertical (y) and horizontal (x) beam profiles are shown in Fig. 3(a) and (b), respectively. With the demagnifying telescope removed, the full OPCPA-output beam caustic was measured using a fixed CaF_2 lens (f=300 mm) and the beam profiler mounted on a motorised translation stage. An M^2 value of 1.4 was correspondingly measured (according to ISO 11146) in both the y and x SWIR-beam axes. The full beam caustic is shown in Fig. 3(c). The y- and x-axis beam profiles recorded at the beam focus are shown in Fig. 3(d) and (e), respectively.

Purging both the OPCPA enclosure and beam transport with N_2 was vital to achieve the reported high spatial beam quality at the HHG chamber. In the regular laboratory air (relative humidity of 35–40%), the M^2 value increases to 2 in both axes. This observation is attributed to 'thermal blooming', whereby a diverging lens forms in air due to absorption by water vapour [42]. The role of high average power was confirmed by observing that the focal beam profile improves when the pulse repetition rate is reduced by a factor of four using the AOPDF. Without purging, the beam exhibits a flat-top profile after a few meters of propagation. It is correspondingly possible that the super-Gaussian profiles shown in Fig. 3(a) and (b) are associated with an insufficient laser and transport-line purge at the time of the measurement.

The pulses are compressed in a pair of low-inclusion, high-homogeneity IR-fused-silica windows, each mounted at ~55° (Brewster's angle at 2.1 μm) but with opposite orientations. This bulk compressor imposes a total GDD of -2000 fs^2, which together with the dispersion in the CaF_2 sampling wedges, focusing lens and vacuum window, results in fully compressed pulses on-target. We found that installing the bulk compressor in the OPCPA enclosure resulted in signs (both spectral and spatial) of significant non-linear propagation, despite the calculated B-integral (assuming a Gaussian beam profile) being <0.5 rad for the bulk compressor and <0.15 rad for transport of the pulses in N_2. These effects are almost completely removed after instead inserting the fused silica compression blocks after ~5 m propagation. However, even in this case, the compressor blocks slightly shift the position of the focus closer to the lens (compared to without the compressor) and make the beam astigmatic, indicating that there is still some self-focusing occurring in the fused-silica blocks. To remove this, it is planned to expand the beam further in the near term, as soon as suitable optics are available.

The pulse temporal profile is measured using a self-referencing spectral interferometry (SRSI) system (Wizzler, Fastlite) coupled to a high-dynamic-range, responsivity corrected SWIR

Optics EXPRESS

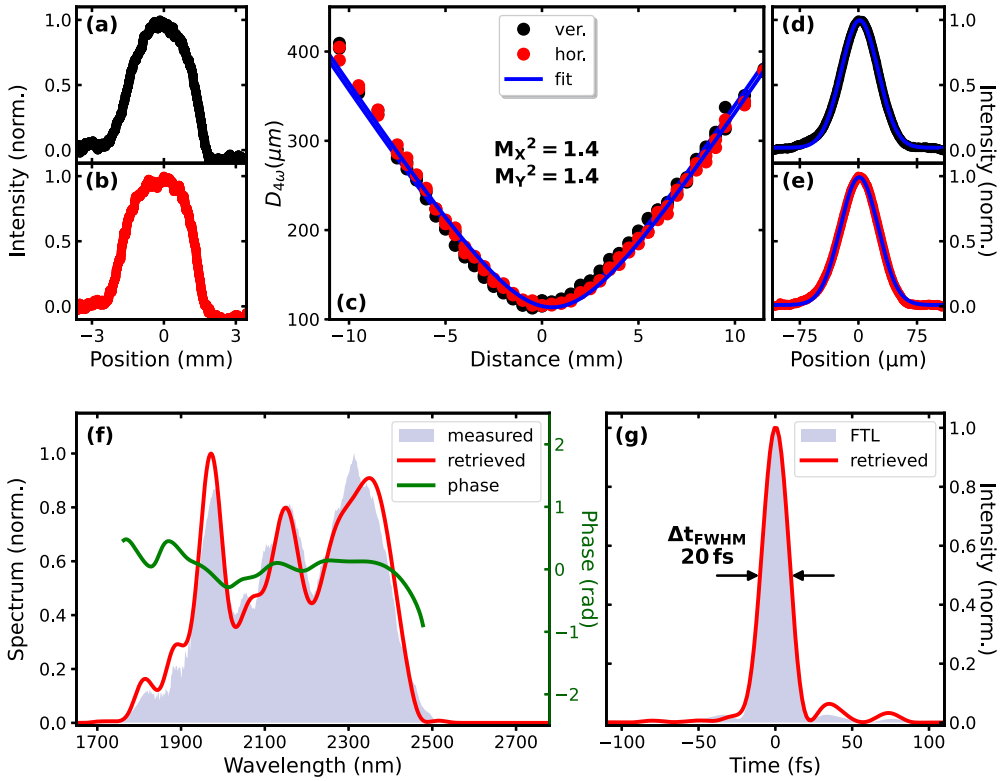

Fig. 3. (a) Vertical and (b) horizontal SWIR beam profiles measured after a 3:1 demagnifying telescope. (c) Beam caustics of the uncompressed SWIR pulses along the vertical (y, black) and horizontal (x, red) directions, as measured using a 300 mm-focal-length lens. The blue lines are the fits used to determine M^2. (d) and (e) respective y- and x-axis intensity profiles at the 0 mm position shown in (c), i.e., at the beam waist. The blue solid lines are Gaussian fits to the profiles. (f) and (g) SRSI-based spectro-temporal characterizations of the compressed SWIR pulses.

spectrum analyzer (Mozza, Fastlite). As shown in Fig. 3(f) and (g), a broadband spectrum and clean temporal profile is retrieved with ~91% of the energy contained within the main, 20 fs FWHM peak (corresponding to 2.9 optical cycles and a 38 fs full-width at tenth-maximum, FWTM, duration). The spectrum reported in Fig. 3(f) differs from the spectrum shown in Fig. 2(d) as the integrating sphere, optical fibre, and InGaAs device used to detect the SFG peak at 1.2 μm has reduced sensitivity beyond 2.2 μm. To obtain optimally compressed pulses, the phase applied by the AOPDF is adjusted with a feedback algorithm informed by successive pulse-characterization measurements, as described in Ref. [43]. Through comparison with the compression results from the OPCPA front end alone, it is determined that the compressed FWHM pulse duration increases only slightly from 19 fs before to 20 fs after the OPCPA-booster stages, demonstrating the preservation of the majority of the seed spectral bandwidth and fine control over the spectral dispersion throughout the high-power-booster section.

A preliminary study of the CEP stabilty after the high-power-booster setup was also undertaken. During these measurements, the fused-silica compression blocks were located in their original position, directly after the collimating mirror following the final OPA stage. Therefore, as outlined above, the pulses underwent significant non-linear propagation before they were sampled for the CEP-stability measurements. An f-2f interferometer, identical to the setup used to characterise the

Optics EXPRESS

OPCPA front end and introduced at the end of Section 2, was installed close to the HHG chamber after ~5 m of propagation. As before, the relative CEP stability was recorded on a single-shot basis at a repetition rate of 13.15 kHz, i.e., every fourth pulse was measured. The results of the measurements are plotted in Fig. 4. Panel (a) shows the relative CEP of the OPCPA front-end, as recorded before the high-power booster development. The associated data demonstrates a shot-resolved CEP noise of 161 mrad RMS over the whole 25-minute measurement period. In contrast, the more recent high-power-booster results plotted in panel (b) show a relatively poor shot-resolved CEP stability of 815 mrad RMS. Since the CEP-stability of the seed pulses can be demonstrated, a likely explanation for the deterioration is the effect of the non-linear propagation that the amplified pulses experienced during temporal compression and propagation to the measurement device. In particular, to generate an octave-spanning spectrum for the CEP measurements, the f-2f interferometer relies on filamentation in a YAG crystal, which is especially sensitive to the spatial profile of the input pulses [35]. Following the downstream shift of the compression blocks and associated improvements in the beam profile and focusability reported above, we expect to measure a significant improvement of the full-OPCPA-output CEP stability.

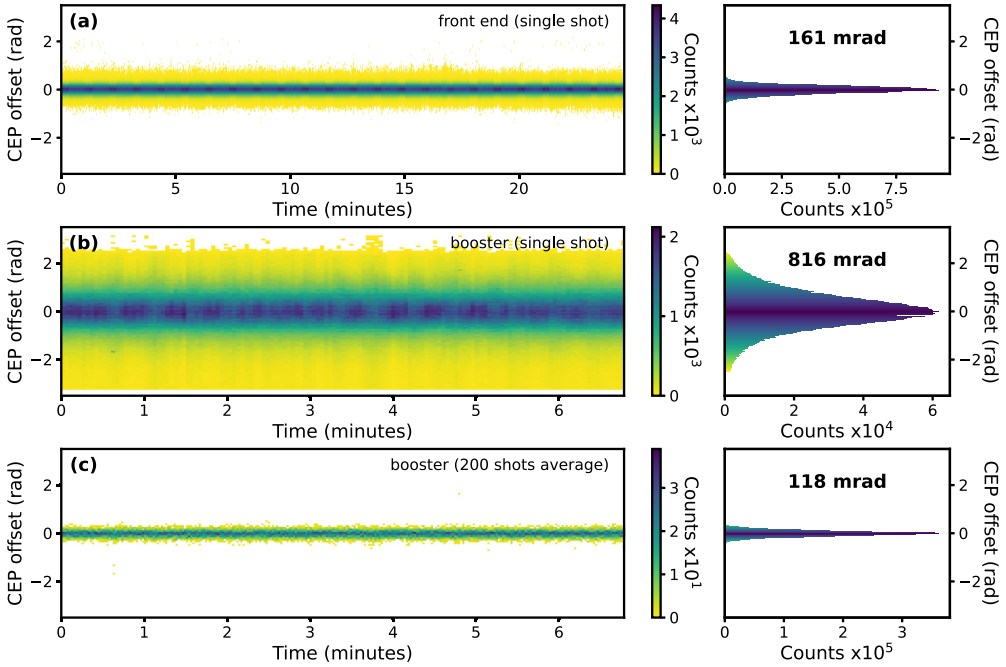

Fig. 4. (left panels) Temporal evolution of the CEP-offset distribution of the SWIR pulses. (a) At the front-end output and (b) at the booster output, as measured with a laser-shot-resolved f-2f interferometer. (c) The data from (b) averaged over 200 shots. (right panels) Histograms of the individual CEP-offset distributions and time-integrated RMS CEP-offset values associated with the corresponding left panels.

In addition to highlighting the potential for CEP-stability degradation in high-power OPCPA systems, the results shown in Fig. 4 also demonstrate the importance of measuring the CEP stability on a single-shot basis. In panel (c), we have plotted the same data shown in panel (b), but now averaged over 200 laser shots. In this case, the apparent relative CEP stability is only 118 mrad RMS. Based only on this averaged data, the CEP stability of our system could be said to be comparable to that measured in Ref. [4] (92 mrad), in which the CEP stability measurements were averaged over 200 shots due to the limited read-out speed of the CEP-measurement devices.

Optics EXPRESS

Under the current conditions, after OPA 5 and ~5 m of propagation via 12 optics – including six SWIR-enhanced mirrors, two CaF_2 beam samplers, two Brewster's-angle fused-silica compression blocks, and two AR-coated CaF_2 chamber windows – the average SWIR power reaching the HHG vacuum chamber is 45 W. The current beam transmission from OPA 5 to the HHG cell correspondingly amounts to ~87%.

5. High-harmonic generation

As a first step towards the goal of realizing a femtosecond-duration, high-photon-flux SXR source extending up to 600 eV, and to test the capabilities of the OPCPA system described here, we have generated high harmonics up to 190 eV in Ar gas. This corresponds to the spectral cutoff for HHG with a 2.1 μm driver with such a target, as previously reported [1,3]. During these tests, the SWIR power was attenuated to 30 W (507 μJ/pulse) by a combination of a broadband, achromatic SWIR waveplate (Newlight Photonics Inc.) and thin-film polariser (Layertec GmbH); this was necessary to enable long-term operation of the currently implemented HHG targets, which have been damaged or destroyed at higher input powers. Further, similar to the CEP-stability measurements, these tests were performed with the bulk IR-fused-silica compressor installed in the OPCPA enclosure, and also without the possibility to transport the beam in an N_2-purged environment. Despite the resulting degraded beam-profile, the HHG demonstration is instructive as a confirmation of the overall performance of the OPCPA as a SXR-HHG driver.

The SXR beamline consisted of a 'HHG' vacuum chamber, containing a pre-drilled, tubular gas cell (diameter 3 mm); a differential pumping assembly; a thin-film-filter array; and a SXR spectrometer system. An AR-coated f=300 mm CaF_2 singlet lens placed before an AR-coated CaF_2 HHG-chamber entrance window was used to focus the SWIR beam into the gas cell. To generate high harmonics, the cell was filled with a variable backing pressure of up to 2 bar of argon. After 1 m of propagation via a pair of differential pumping apertures, the high-power SWIR beam was separated from the SXR beam by a 200 nm-thick silver filter mounted on a thermally conductive copper mesh with a 254 μm pitch (Luxel Corporation). The filter was aligned at 45° to reflect most of the residual SWIR light out of the beamline via a vacuum window and positioned between a pair of SWIR-beam baffles that were used to minimize further propagation of any residual SWIR light. The implemented filter angle results in an effective SXR pathlength of 283 nm through Ag.

We used a commercial SXR spectrometer (EVEREST, Ultrafast Innovations GmbH) in combination with an X-ray CCD camera (ALEXs 2k512 BI UV, Great Eyes GmbH) to record spatially-resolved spectra of the SXR emission. The result is shown in Fig. 5(a). The absence of discrete peaks can be explained by the limited detection resolution (no spectrometer entrance slit was installed for these measurements) together with the narrow high-harmonic spacing expected from a 2.1 μm driver. Through comparison with data recorded with lower-power SWIR input beams and alternative metallic filters without Cu-mesh supports, the vertical discontinuities in Fig. 5(a) can be attributed to the Cu-grid support on the implemented Ag filter. Based on beamline ray tracing simulations and the known detection efficiency of the X-ray camera, we estimate the photon flux at 150 eV to be $\sim 9 \times 10^6$ ph/s/eV. This value is greater than the photon flux originally reported from the 27 W, 2.1 μm system described in Ref. [3], but is around two orders of magnitude lower than the optimized value that was later obtained with the same system [44]. Therefore, after the improvements to the spatial profile described in the previous section and further optimization of the SXR-generation conditions, we expect to significantly increase the generated SXR photon flux.

Optics EXPRESS

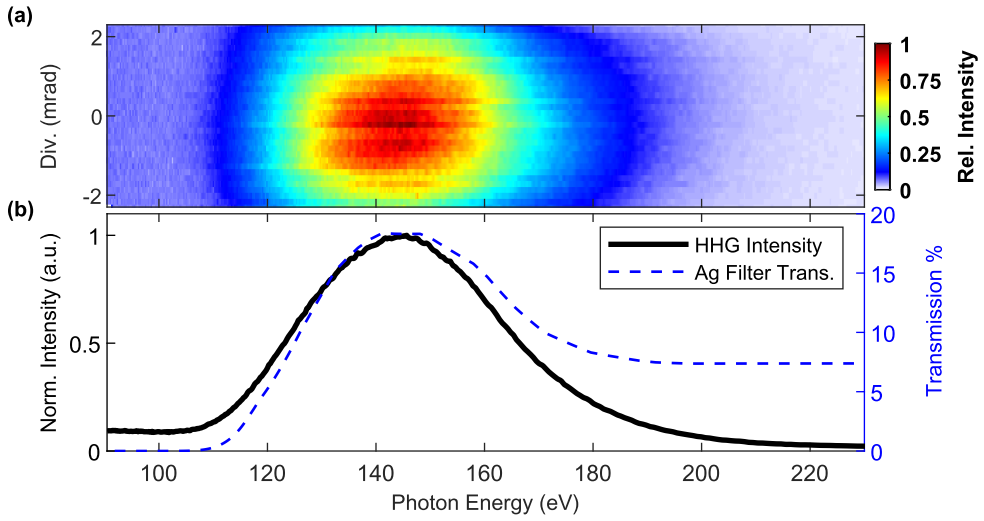

Fig. 5. (a) Spatially resolved HHG spectra obtained from OPA 5. (b) Intensity-normalized spectra extracted from the camera image shown in (a). The blue-dotted line shows the expected transmission of an Ag filter on a supporting Cu mesh with an effective thickness of 283 nm, as implemented to collect the data. Div. refers to the horizontal beam divergence of the HHG source.

6. Conclusion

We have demonstrated a high-average power (52 W), few-optical-cycle SWIR OPCPA system delivering ~0.9 mJ, 2.1 μm and 20 fs pulses at 52.6 kHz (45 W) to a rare-gas-filled cell, enabling the generation of SXR high harmonics. The spectral and polarization purity, energy and power stability, and beam caustics of the OPCPA output pulses have been demonstrated. Characterization of the OPCPA-output pulses after temporal compression and propagation to the HHG chamber reveals an excellent temporal profile (20 fs, 91% of the energy in the main peak), good focusability (M^2 ~1.4), and moderate single-shot CEP stability (820 mrad RMS). These properties enabled the demonstration of HHG driven by 30 W of average power up to the expected SWIR-driving-wavelength cut-off in argon gas, thereby positioning the system at the forefront of currently available drivers for table-top SXR generation.

The developed SWIR-OPCPA system offers multiple opportunities for further improvements, for example, by implementing higher performance AR coatings on the OPCPA crystals, slightly increasing the beam size prior to temporal compression, and remeasuring the CEP-stability after shifting the compressor optics towards the system diagnostics and HHG chamber. Such enhancements will be particularly important for optimally efficiently driving higher-order HHG processes in neon and helium gas targets and the maximization of the SXR flux across the water transparency window. Irrespective of such improvements, the developed laser already achieves the requisite specifications to produce a high-repetition-rate, spectroscopically useful source of ultrashort SXRs up to ~600 eV photon energies. Correspondingly, it can be considered an enabling technology for ultrafast and chemical-site-specific investigations of electronic-structure dynamics, particularly in complex, condensed-phase environments.

Funding. Helmholtz-Zentrum Berlin für Materialien und Energie; Eurostars (E! 113566).

Acknowledgements. The authors gratefully acknowledge the support of Mr. Pascal Tournois, Mr. Thomas Pinoteau and Dr. Alexander Guggenmos throughout the laser- and SXR-source-development projects. Expert support was received from Dr. Mojtaba Hajialamdari and Dr. Siqi Cheng with the optimization of the pump laser. Stimulating technical discussions with Prof. Albert Stolow, Dr. Andrey Boguslavskiy, and Dr. Rune Lausten are also gratefully

Optics EXPRESS

acknowledged. The authors also express their gratitude to the HZB Technical Design & Manufacturing and Facility Management departments for their respective assistance in realizing the laser enclosure and associated laboratory space.

Disclosures. FASTLITE is a commercial company that sells ultrafast-laser devices and OPCPA lasers. Ultrafast Innovations is a commercial company that sells ultrafast-laser optics and devices. Otherwise, the authors declare no conflicts of interest.

Data availability. Data underlying the results presented in this paper are not publicly available at this time but may be obtained from the authors upon reasonable request.

References

1. G. J. Stein, P. D. Keathley, P. Krogen, *et al.*, "Water-window soft x-ray high-harmonic generation up to the nitrogen K-edge driven by a kHz, 2.1 µm OPCPA source," J. Phys. B: At., Mol. Opt. Phys. **49**(15), 155601 (2016).
2. J. Pupeikis, P.-A. Chevreuil, N. Bigler, *et al.*, "Water window soft x-ray source enabled by a 25 W few-cycle 2.2 μm OPCPA at 100 kHz," Optica **7**(2), 168 (2020).
3. T. Feng, A. Heilmann, M. Bock, *et al.*, "27 W 2.1 μm OPCPA system for coherent soft X-ray generation operating at 10 kHz," Opt. Express **28**(6), 8724 (2020).
4. M. F. Seeger, D. Kammerer, J. Blöchl, *et al.*, "49 W carrier-envelope-phase-stable few-cycle 2.1 µm OPCPA at 10 kHz," Opt. Express **31**(15), 24821 (2023).
5. M.-C. Chen, P. Arpin, T. Popmintchev, *et al.*, "Bright, coherent, ultrafast soft x-ray harmonics spanning the water window from a tabletop light source," Phys. Rev. Lett. **105**(17), 173901 (2010).
6. A. D. Shiner, C. Trallero-Herrero, N. Kajumba, *et al.*, "Wavelength scaling of high harmonic generation efficiency," Phys. Rev. Lett. **103**(7), 073902 (2009).
7. S. M. Teichmann, F. Silva, S. L. Cousin, *et al.*, "0.5-keV Soft X-ray attosecond continua," Nat. Commun. **7**(1), 11493 (2016).
8. X. Ren, J. Li, Y. Yin, *et al.*, "Attosecond light sources in the water window," J. Opt. **20**(2), 023001 (2018).
9. D. Popmintchev, B. R. Galloway, M.-C. Chen, *et al.*, "Near- and extended-edge x-ray-absorption fine-structure spectroscopy using ultrafast coherent high-order harmonic supercontinua," Phys. Rev. Lett. **120**(9), 093002 (2018).
10. A. S. Johnson, D. R. Austin, D. A. Wood, *et al.*, "High-flux soft x-ray harmonic generation from ionization-shaped few-cycle laser pulses," Sci. Adv. **4**(5), eaar3761 (2018).
11. C. Schmidt, Y. Pertot, T. Balciunas, *et al.*, "High-order harmonic source spanning up to the oxygen K-edge based on filamentation pulse compression," Opt. Express **26**(9), 11834 (2018).
12. V. Cardin, B. E. Schmidt, N. Thiré, *et al.*, "Self-channelled high harmonic generation of water window soft x-rays," J. Phys. B: At., Mol. Opt. Phys. **51**(17), 174004 (2018).
13. Y. Fu, K. Nishimura, R. Shao, *et al.*, "High efficiency ultrafast water-window harmonic generation for single-shot soft X-ray spectroscopy," Commun. Phys. **3**(1), 92 (2020).
14. L. Barreau, A. D. Ross, S. Garg, *et al.*, "Efficient table-top dual-wavelength beamline for ultrafast transient absorption spectroscopy in the soft X-ray region," Sci. Rep. **10**(1), 5773 (2020).
15. T. Popmintchev, M. C. Chen, D. Popmintchev, *et al.*, "Bright coherent ultrahigh harmonics in the keV x-ray regime from mid-infrared femtosecond lasers," Science **336**(6086), 1287–1291 (2012).
16. A. R. Attar, A. Bhattacherjee, C. D. Pemmaraju, *et al.*, "Femtosecond x-ray spectroscopy of an electrocyclic ring-opening reaction," Science **356**(6333), 54–59 (2017).
17. N. Saito, H. Sannohe, N. Ishii, *et al.*, "Real-time observation of electronic, vibrational, and rotational dynamics in nitric oxide with attosecond soft x-ray pulses at 400 eV," Optica **6**(12), 1542 (2019).
18. T. P. Sidiropoulos, N. Di Palo, D. E. Rivas, *et al.*, "Probing the energy conversion pathways between light, carriers, and lattice in real time with attosecond core-level spectroscopy," Phys. Rev. X **11**(4), 041060 (2021).
19. B. Buades, A. Picón, E. Berger, *et al.*, "Attosecond state-resolved carrier motion in quantum materials probed by soft x-ray XANES," Appl. Phys. Rev. **8**(1), 011408 (2021).
20. C. Kleine, M. Ekimova, G. Goldsztejn, *et al.*, "Soft X-ray absorption spectroscopy of aqueous solutions using a table-top femtosecond soft x-ray source," J. Phys. Chem. Lett. **10**(1), 52–58 (2019).
21. C. Kleine, M. Ekimova, M.-O. Winghart, *et al.*, "Highly efficient soft x-ray spectrometer for transient absorption spectroscopy with broadband table-top high harmonic sources," Struct. Dyn. **8**(3), 034302 (2021).
22. A. G. Ciriolo, R. Martínez Vázquez, G. Crippa, *et al.*, "Microfluidic devices for quasi-phase-matching in high-order harmonic generation," APL Photonics **7**(11), 110801 (2022).
23. T. Kroh, C. Jin, P. Krogen, *et al.*, "Enhanced high-harmonic generation up to the soft X-ray region driven by mid-infrared pulses mixed with their third harmonic," Opt. Express **26**(13), 16955 (2018).
24. L. Hareli, G. Shoulga, and A. Bahabad, "Phase matching and quasi-phase matching of high-order harmonic generation-a tutorial," J. Phys. B: At., Mol. Opt. Phys. **53**(23), 233001 (2020).
25. N. Thiré, R. Maksimenka, B. Kiss, *et al.*, "Highly stable, 15 W, few-cycle, 65 mrad CEP-noise mid-IR OPCPA for statistical physics," Opt. Express **26**(21), 26907 (2018).
26. M. K. R. Windeler, K. Mecseki, A. Miahnahri, *et al.*, "100 W high-repetition-rate near-infrared optical parametric chirped pulse amplifier," Opt. Lett. **44**(17), 4287 (2019).
27. Z. Wang, T. Heuermann, M. Gebhardt, *et al.*, "Nonlinear pulse compression to sub-two-cycle, 1.3 mJ pulses at 1.9 μm wavelength with 132 W average power," Opt. Lett. **48**(10), 2647 (2023).

Optics EXPRESS

28. L. Xu and E. J. Takahashi, "Dual-chirped optical parametric amplification of high-energy single-cycle laser pulses," Nat. Photonics **18**(1), 99–106 (2024).
29. C. Manzoni and G. Cerullo, "Design criteria for ultrafast optical parametric amplifiers," J. Opt. **18**(10), 103501 (2016).
30. H. Fattahi, H. G. Barros, M. Gorjan, *et al.*, "Third-generation femtosecond technology," Optica **1**(1), 45 (2014).
31. A. Giree, M. Mero, G. Arisholm, *et al.*, "Numerical study of spatiotemporal distortions in noncollinear optical parametric chirped-pulse amplifiers," Opt. Express **25**(4), 3104 (2017).
32. J. Rothhardt, S. Demmler, S. Hädrich, *et al.*, "Thermal effects in high average power optical parametric amplifiers," Opt. Lett. **38**(5), 763 (2013).
33. J. H. Buss, S. Starosielec, M. Schulz, *et al.*, "Mid-infrared optical parametric chirped-pulse amplifier at 50 W and 38 fs pumped by a high-power Yb-InnoSlab platform," Opt. Express **32**(21), 36185–36192 (2024).
34. R. Maksimenka, G. Jargot, N. Thiré, *et al.*, "Ultra-stable opcpa at 2 μm, 16 fs, sub 100 mrad cep noise," in *OSA High-brightness Sources and Light-driven Interactions Congress 2020 (EUVXRAY, HILAS, MICS)*, (Optica Publishing Group, 2020), p.MM1C.3.
35. B. Maingot, N. Forget, and A. Jullien, "Spatial-to-spectral phase coupling mechanisms in bulk continuum generation," J. Phys. Photonics **6**(3), 035002 (2024).
36. B. Mahieu, D. Gauthier, X. Ge, *et al.*, "Spatial quality improvement of a Ti:Sapphire laser beam by modal filtering," Appl. Phys. B **118**(1), 47–60 (2015).
37. Z. Su, Q. Meng, and B. Zhang, "Analysis on the damage threshold of MgO:$LiNbO_3$ crystals under multiple femtosecond laser pulses," Opt. Mater. **60**, 443–449 (2016).
38. J. Rams, A. Alcázar-De-Velasco, M. Carrascosa, *et al.*, "Optical damage inhibition and thresholding effects in lithium niobate above room temperature," Opt. Commun. **178**(1-3), 211–216 (2000).
39. R. Maksimenka, T. Pinoteau, N. Forget, *et al.*, "High-average power, soft x-ray generation driver at 2.1 μm," in *Conference on Lasers and Electro-Optics/Europe (CLEO/Europe 2023) and European Quantum Electronics Conference (EQEC 2023)*, (Optica Publishing Group, 2023), p.cg_p_16.
40. K. Mecseki, M. K. R. Windeler, A. Miahnahri, *et al.*, "High average power 88 W OPCPA system for high-repetition-rate experiments at the LCLS x-ray free-electron laser," Opt. Lett. **44**(5), 1257 (2019).
41. J. Bromage, J. Rothhardt, S. Hädrich, *et al.*, "Analysis and suppression of parasitic processes in noncollinear optical parametric amplifiers," Opt. Express **19**(18), 16797 (2011).
42. B. Hafizi, J. Pe nano, R. Fischer, *et al.*, "Determination of absorption coefficient based on laser beam thermal blooming in gas-filled tube," Appl. Opt. **53**(22), 5016 (2014).
43. S. Grabielle, A. Moulet, N. Forget, *et al.*, "Self-referenced spectral interferometry cross-checked with spider on sub-15fs pulses," Nucl. Instrum. Methods Phys. Res., Sect. A **653**(1), 121–125 (2011).
44. M. van Mörbeck-Bock, T. Feng, A. Heilmann, *et al.*, "High average power OPCPA MIR-systems for coherent soft x-ray generation accessing absorption edges of metals," *High Power Lasers and Applications*, vol. 11777 J. Hein, T. J. Butcher, P. Bakule, *et al.*, eds., International Society for Optics and Photonics (SPIE, 2021), p. 117770C.